High-resolution CMOS imaging detector

Thorsten Graeve and Gene P. Weckler
Rad-icon Imaging Corp.

ABSTRACT

A 2.5 cm by 5 cm, 512 by 1024 pixel CMOS photodiode array detector designed specifically for digital radiography will be described. All necessary scanning and readout circuitry is integrated within the detector. The small pixel spacing of 48 µm allows the imager to easily achieve the 10 lp/mm resolution required for the targeted interventional mammography application. Direct coupling to the scintillator and a pixel fill factor of more than 80% leads to high DQE over a large range of exposure values. The detector exhibits very low dark current of about 30 pA/cm^2 at room temperature, which allows for low-noise operation and long integration times. Read noise of less than 200 electrons rms and a saturation level of 2.8×10^6 electrons combine for a large dynamic range greater than 80 dB. The conversion gain of the detector is 0.5 µV/electron. Combined with a Gd_2O_2S scintillator, the imager achieves up to 25% MTF at 10 lp/mm and a DC detective quantum efficiency of 50%. The detector design is optimized for x-ray energies between 10 kV and 50 kV, but can be retrofitted with different scintillator screens to cover a large range of imaging applications up to 160 kV.

Keywords: CMOS detector, photodiode array, active pixel sensor, x-ray imaging, digital radiography.

1. INTRODUCTION

Imaging detectors for digital radiography have started to come of age over the past few years. Besides the large-area flat panel detectors for general radiography, there has also been much activity focussed on high-resolution detectors for digital mammography. These systems usually require between 5 and 10 lp/mm resolution, and often feature smaller input windows designed for imaging a specific region-of-interest. Although some of this research has been based on amorphous silicon[1] or amorphous selenium[2,3] flat panel detectors, most systems to date feature a charge-coupled device (CCD) sensor that is either lens-coupled[4-8] or connected via a fiber-optic taper[9-14] to an input phosphor screen. There are also several studies that compare and contrast the merits of these last two approaches.[15-17]

Amorphous silicon imagers are photodiode arrays with a thin-film transistor (TFT) readout switch at each pixel. The thin-film technology makes possible the use of very large imaging areas (up to 40 cm). Another advantage of amorphous silicon is the high radiation tolerance. However, it has limitations in both resolution (typically at least 100 µm pixel size) and performance (most notably noise and image lag) due to the less-than-ideal properties of the amorphous silicon semiconductor. In addition, amorphous silicon imagers require a specialized fabrication process with a dedicated manufacturing facility, increasing both production and development costs relative to competing technologies.

CCD imagers are the established leading technology for high-performance optical imaging. Unlike matrix-addressed imagers like amorphous silicon panels and CMOS imagers, CCDs read out their signal by transporting charge packets across the silicon substrate. Their advantages include high resolution, low noise and high sensitivity. In digital radiography, they are usually combined with a fiber-optic taper that increases the field-of-view and protects the CCD from radiation. CCDs are very sensitive to radiation damage, and even with the added shielding of the taper they can only be used in low-energy x-ray imaging applications (typically less than 50 kV). As with amorphous silicon, their production requires a specialized process that adds to their development cost. The fiber-optic taper is also costly, difficult to interface to the CCD chip, and significantly decreases the CCD's sensitivity.

CMOS imagers, like amorphous silicon panels, are matrix-addressed photodiode arrays. They take advantage of a highly developed manufacturing infrastructure – the semiconductor industry – by using the same fabrication processes and equipment that is used to make microprocessors and logic arrays. In other words, the IC industry has already paid for the technology development and fabrication equipment, and is continuing to do so. Today's small-linewidth processes allow the

Contact Information:
E-mail: tgraeve@rad-icon.com; gpweckler@rad-icon.com; phone: 408-486-0886; fax: 408-486-0882
Rad-icon Imaging Corp, 3193 Belick Street, Unit 1, Santa Clara, CA 95054-2404; http://www.rad-icon.com

Copyright 2001 Society of Photo-Optical Instrumentation Engineers. This paper has been published in *Medical Imaging 2001 – Physics of Medical Imaging*, SPIE Vol. 4320, and is made available as an electronic reprint with permission of SPIE. One print or electronic copy may be made for personal use only. Systematic or multiple reproduction, distribution to multiple locations via electronic or other means, duplication of any material in this paper for a fee or for commercial purposes, or modification of the content of the paper are prohibited.

addition of special features on a per-pixel basis, vastly improving the performance of the CMOS array. Noise levels comparable to CCDs can now be achieved, and the saturation capacity of a CMOS imager is usually several times larger than that of a CCD. CMOS technology also makes it possible to integrate imaging, timing and readout functions all on the same device. The highly integrated architecture allows the design of a “system on a chip”, which is ultimately less costly than an imager requiring a large amount of support electronics.

Rad-icon Imaging Corp. developed the RadEye1 CMOS image sensor to leverage the advantages of CMOS technology into developing a detector suitable for digital radiography. The pixel size and active area are specifically designed for interventional mammography and similar biopsy applications. With today’s CMOS technology the detector can be made large enough to allow direct, contact imaging of the scintillator, thus avoiding the signal losses and other difficulties associated with lens coupling or fiber-optic tapers. The device read noise is nearly an order of magnitude lower than that of an amorphous silicon panel, enabling photon-noise limited operation even at low x-ray energies. The following sections discuss the first in-depth characterization of this detector in terms of light properties, dark current, MTF and DQE. A number of imaging examples will be presented to illustrate potential applications.

2. DESCRIPTION

The RadEye1 image sensor, shown in Figure 1, consists of a two-dimensional array of photodiodes along with CMOS structures for scanning and readout. The 24.6 mm by 49.2 mm active area contains a 512 by 1024 photodiode matrix with 48 µm spacing. All support and control functions are integrated on-chip. The device is three-side buttable, allowing multiple sensors to be tiled together to achieve larger image formats.

Figure 2 shows a summary of the device specifications. The RadEye1 detector features a large saturation signal capacity of nearly three million electrons, yet has less than 200 electrons of dark noise. The resulting dynamic range exceeds 83 dB (14,000:1). At room temperature, the per-pixel dark current of less than 10,000 electrons per second allows integration times of several tens of seconds without saturating the device. For near real-time applications, the maximum readout rate of 2.5 MHz enables a top frame rate of 4.5 frames per second.

The RadEye1 offers several imaging modes, including a standard output mode, a non-destructive readout mode, and a high-speed, low resolution sparse-sampling mode in which only every other row and column is sampled. In the simplest readout mode, only a 5 V power supply, a reference voltage and an external pixel clock are required to continuously output frames from the device. The frame rate can be controlled either by adjusting the pixel clock frequency or by supplying an external start pulse that triggers the beginning of each readout sequence. Additional control inputs add further flexibility to the readout process in order to synchronize the detector to an x-ray source.

The RadEye1 imager can be used by itself as a visible light detector, or with a direct-coupled scintillator as an x-ray detector. Due to the large device area, it is difficult to couple a fiber-optic plate or similar stiff, inflexible scintillator module to the

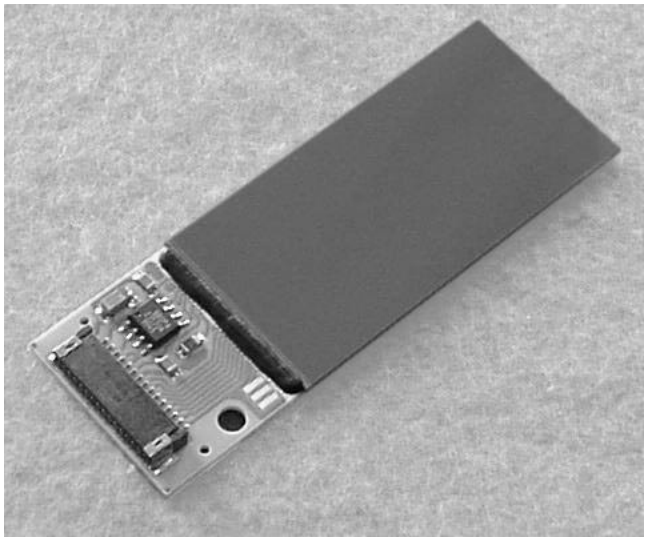

Figure 1a – RadEye1 CMOS image sensor.

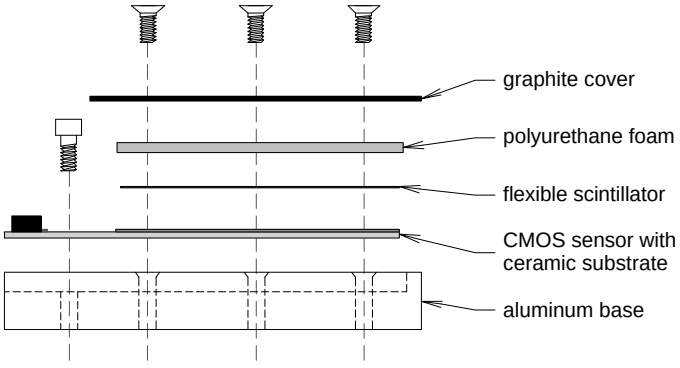

Figure 1b – Cross section with scintillator.

detector. Scintillators with flexible plastic backing or direct-deposited scintillators give the best result in terms of uniform coupling efficiency and resolution. For this study, the RadEye1 imager was tested either using visible light or with a flexible, rare-earth scintillator screen (Gd_2O_2S:Tb) in direct contact with the active area. The scintillator was held against the detector using a thin polyurethane foam layer for compression, and a 1 mm thick graphite cover (see Figure 1b). No coupling fluids were used.

The active area of the RadEye1 extends to within less than 50 µm of the die edge on three sides of the device. This allows tiling the detector into larger mosaics, leaving only a two-pixel gap between the individual pieces. A one by two mosaic, resulting in a 5 cm by 5 cm active area, is already in production. Larger one by four (5 cm by 10 cm) and two by four (10 cm by 10 cm) mosaics are also possible. Since all devices in a mosaic would operate in parallel, the cumulative data rate of the imager increases, and the frame rate remains the same as that of a single RadEye1 device by itself.

Dark Current (each pixel)	< 10^4 electrons/sec
Read Noise (at 1 fps)	< 200 electrons
Saturation	2,800,000 electrons
Dynamic Range	> 10,000:1
Frame Rate	0.01 to 4.5 fps
Max. Data Rate	2.5 MHz
Conversion Gain	0.5 µV/electron
Supply Voltage (VDD)	5 V (±0.25 V)
Supply Current	25 mA (typ)
Reference Voltage (VD)	3.8 V (±0.5 V)
Analog Output +	2 V (dark) to 2.7 V (sat)
Analog Output –	2 V (dark) to 1.3 V (sat)
Digital "low" Voltage	0.5 V max.
Digital "high" Voltage	4.5 V min.
Operating Temperature	0 to 50 °C
Storage Temperature	-25 to +85 °C

Figure 2 – RadEye1 Specifications.

3. MEASUREMENTS

We performed an extensive characterization of the RadEye1 device to determine its operating characteristics both as a visible light imager and with various scintillators as an x-ray image sensor. For the light measurements the sensor was illuminated with a pulsed green LED source. A 12-bit data acquisition board (National Instruments PCI-6111E) was used to generate the timing pulses and acquire the analog signal from the sensor. The x-ray measurements were performed by mounting the RadEye1 sensor inside a Shad-o-Box camera also manufactured by Rad-icon Imaging Corp. This camera also digitizes the output video to 12 bits and transfers the image data to a PC via a digital frame grabber. The acquired image data were divided by the camera gain of 250 µV/ADU to refer the signal back to the output of the RadEye1 sensor. The x-ray source used for the measurements was an Oxford XTC5010 with a Tungsten target and 0.5 mm Al filtration. Most measurements were taken at a source setting of 30 kV.

3.1. Light Response and Dynamic Range

The light response of the RadEye1 sensor was measured by increasing the pulse width of the illuminating green LED in even steps until the output signal from the sensor leveled off. Since the imager is scanned in a row-sequential format, the light pulses were timed to fall into the blanking interval in between frame readouts to ensure equal illumination of all pixels. The output signal was then averaged over a small 100x100 pixel region-of-interest (ROI) to minimize the effects of non-uniformity in the illumination. Figure 3 shows the resulting response curve. Note that the input signal was not independently calibrated. Small variations in the light pulses, for example due to heating of the LED, have not been corrected.

We measured the conversion gain of the RadEye1 detector by employing the well-known mean-variance method.[18] Sets of two subsequent exposures were taken for a range of LED illumination levels. The mean signal was obtained by averaging over a 200x200 pixel ROI. The variance at each signal level was then calculated from the difference image over the same ROI in order to eliminate any fixed pattern offsets. The resulting plot is shown in Figure 4.

3.2. Dark Current

The dark current was measured by taking two dark exposures, typically at one second and five seconds integration time. The difference between the two images, divided by the difference in integration time and by the conversion gain, yields the dark current for each pixel in electrons per second. Figure 5 shows a distribution of dark current measurements at room temperature for the RadEye1 sensor. The average dark current is just over 4000 electrons per second, which corresponds to about 30 pA/cm^2. Figure 6 shows how the average dark current varies with temperature over the extended operating range of the device. The exponential fit to the data shows that the dark current doubles every 8.1 °C.

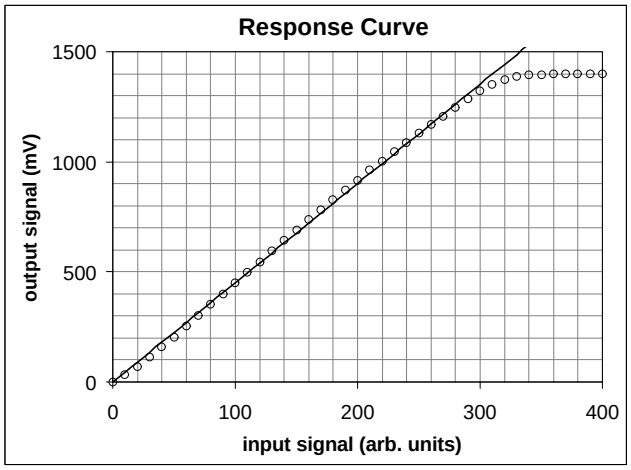

Figure 3 - RadEye1 response to visible light (pulsed green LED).

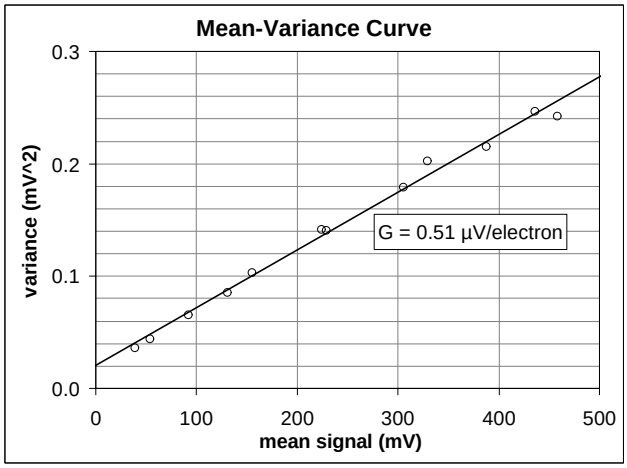

Figure 4 – Mean-variance curve for visible light input (pulsed green LED).

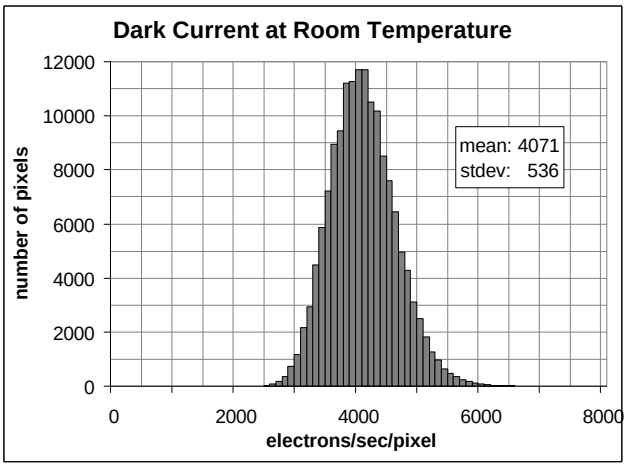

Figure 5 – Dark current distribution at 23°C. The mean dark current corresponds to approximately 30 pA/cm^2.

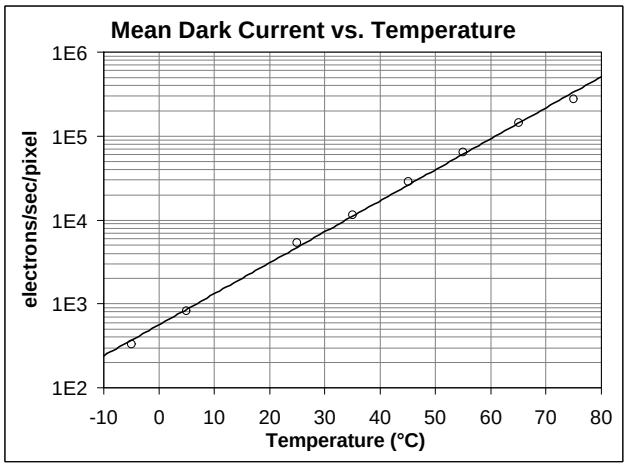

Figure 6 – Dark current as a function of substrate temperature. The dark current doubles every 8°C.

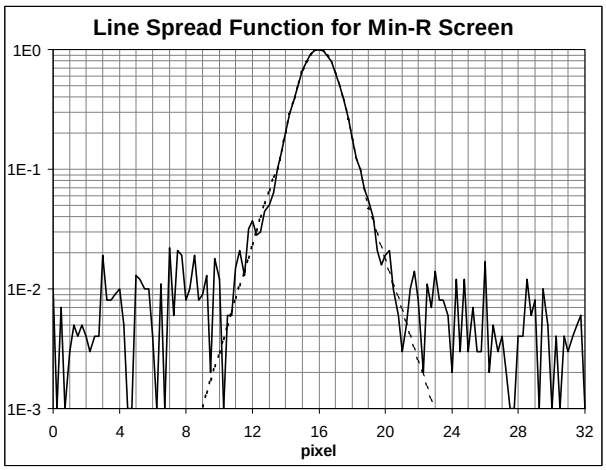

Figure 7 – Normalized LSF from step image with 4 times oversampling. Dashed lines indicate the extrapolated tails.

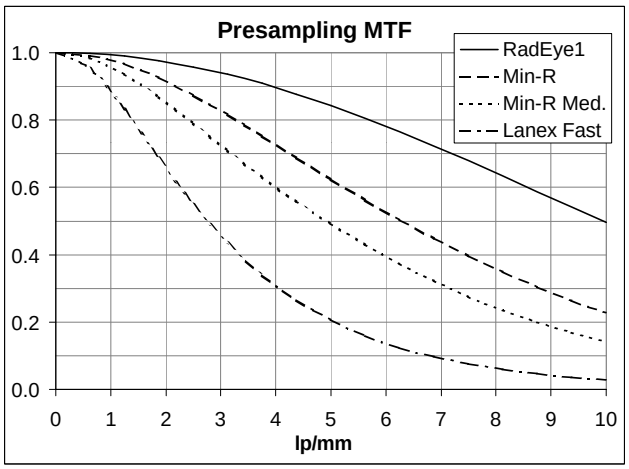

Figure 8 – Presampling MTF for the bare RadEye1 detector and with three different Gd_2O_2S scintillators.

3.3. Modulation Transfer Function

The MTF of the RadEye1 imager was measured using the techniques described by Judy[19] and Reichenbach.[20] A straight ceramic edge, angled slightly with respect to the column direction, was placed in the x-ray beam to obtain an image of a step function. The line spread function (LSF) was obtained by shifting each row a fraction of a pixel to line up the edge locations, averaging across a large number of rows, and then differentiating the result. The tails of the LSF were extended below the noise floor of the detection system using an exponential fit. This both smoothes out the resulting MTF curve and helps to remove artifacts caused by truncating the LSF at the noise floor.[21] A normalized line spread function along with the extrapolated tails is shown in Figure 7. The modulus of the Fourier transform of the LSF then yields the presampling modulation transfer function. Figure 8 shows the presampling MTF of the RadEye1 detector by itself (measured using direct detection of x-rays in the silicon), and with three different scintillators that were placed in direct contact with the imager. We did not observe any difference between MTF curves measured along the row- vs. the column-direction of the sensor.

3.4. Detective Quantum Efficiency

The RadEye1 DQE, using the Min-R Medium scintillator, was calculated both at DC and as a function of spatial frequency. The first case can be written as

$$DQE(0) = (V_{out}^2 / \sigma^2) \cdot 1/q = G^2 \cdot q / \sigma^2. \qquad (1)$$

where G is the average conversion gain in mV/photon, or simply V_{out}/q; q is the number of x-ray photons per pixel incident on the detector during one integration period; and σ^2 is the variance in the output signal. V_{out} and σ^2 were measured directly from x-ray images taken at various exposure levels. The quantum fluence q was estimated based on published tables of x-ray emission spectra.[22,23] Figure 9 shows a plot of DQE(0) calculated for several signal levels.

In order to calculate DQE(f) the noise power spectrum has to be known. The NPS was obtained from the image data by applying the direct Fourier transform method[24,25] along one dimension and then averaging along the other. The resulting plots are shown in Figure 10 for several different exposure levels. The DQE is then simply given by

$$DQE(f) = G^2 \cdot q \cdot MTF(f)^2 / NPS(f). \qquad (2)$$

The resulting curves of DQE(f) are shown in Figure 11.

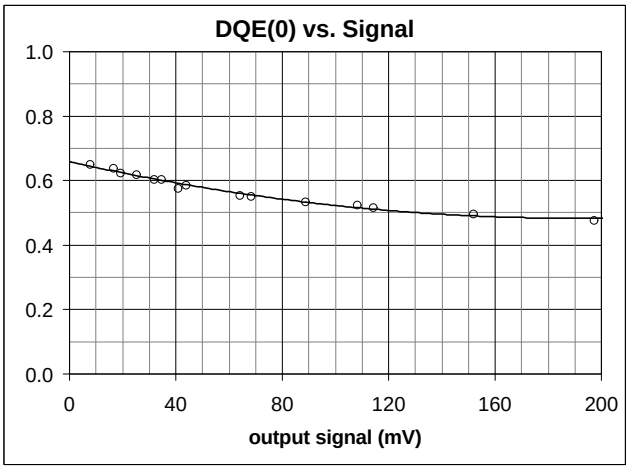

Figure 9 – DQE(0) as calculated from the image mean and variance, and the estimated quantum fluence.

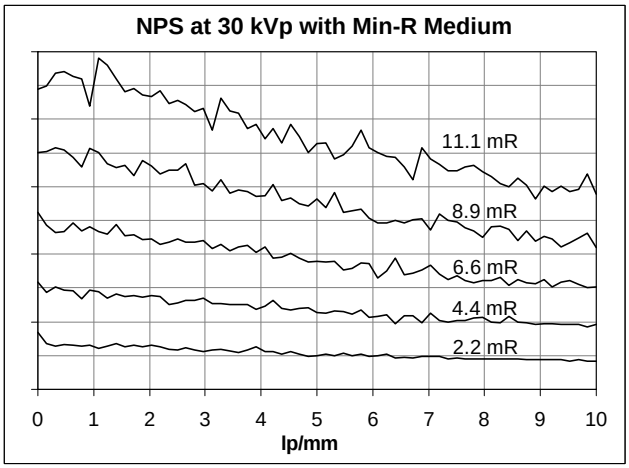

Figure 10 – NPS at different exposure levels.

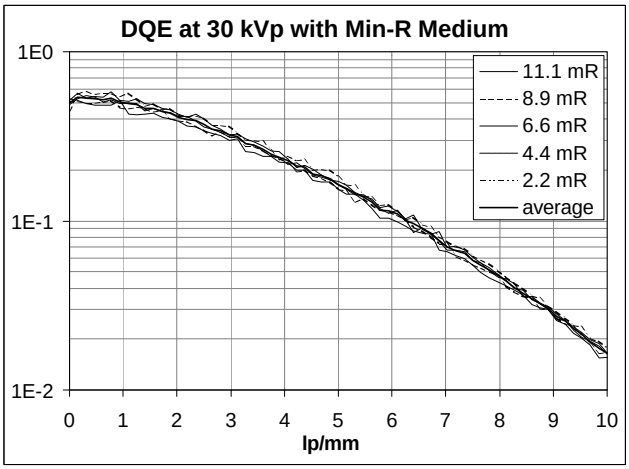

Figure 11 – Frequency-dependent DQE from equation (2), using data from Figures 8 and 10.

4. DISCUSSION

4.1. Light Response and Dynamic Range

Figure 3 shows the light response of the RadEye1 sensor. Since the RadEye1 device uses a voltage-pickoff architecture, the signal response is inherently less linear than that of a charge-readout device. However, the advantages of the voltage-pickoff circuit are lower noise, extended dynamic range, and faster readout. Figure 3 shows small deviations of up to 1% of the saturation signal from the ideal linear response curve. The detector saturates at about 1400 mV, or 2.8×10^6 electrons.

The sensing and readout circuitry of the RadEye1 detector uses a pixel capacitance of approximately 0.15 pF and a total voltage gain from pixel to output of about 0.51 V/V. The theoretical conversion gain is therefore 0.54 µV/electron. Assuming Poisson statistics and photon-noise limited operation, the slope of the mean-variance curve in Figure 4 is equal to the inverse of the conversion gain of the detector. From the plot we calculated the actual conversion gain to be 0.51 µV/electron. The slight gain non-uniformity seen in the response curve of Figure 3 is also evident in this plot. The estimated rms dark noise, given by the y-intercept of the mean-variance plot, comes out to 280 electrons. This number is actually dominated by the read noise of the data acquisition system used for this test. By subtracting out this noise, we estimate that the intrinsic dark noise of the RadEye1 detector is less than 200 electrons.

1.2. Modulation Transfer Function

As seen in Figure 8, the presampling MTF of the bare RadEye1 imager as a direct x-ray detector is very close to the theoretical maximum. Both the Kodak Min-R Regular and Min-R Medium screens deliver quite satisfactory results (the newer Min-R 2000 and Min-R 2190 screen were not available for this study). However, a Lanex Fast screen will obviously not take advantage of the high intrinsic resolution of the detector.

The exponential extrapolation technique used in determining the presampling MTF curves tends to slightly skew the plots towards the lower spatial frequencies. By eliminating the noise floor, the resulting MTF curves are higher at the low spatial frequencies and slightly lower at the cutoff frequency. Unfortunately, a rather short exposure was used to acquire the edge images for the MTF calculations. As a result, the LSF plots contain a useful dynamic range of only about 100:1. A high-contrast exposure that takes full advantage of the RadEye1's dynamic range would yield a more accurate estimate. The estimated error in the curves in Figure 8 is on the order of ±5%.

1.3. Detective Quantum Efficiency

Using equation (1) to estimate DQE(0) has the advantage that two of the three relevant parameters can be measured directly from the output image delivered by the detector. Unfortunately, it also requires knowledge of parameter q, the quantum fluence, which can be difficult to estimate. Although tables of emission spectra can be found in the literature that allow q to be calculated, these numbers are highly dependent on the true kVp of the x-ray source and the type and amount of filtration used. The data shown in Figures 9 and 11 are therefore intended to be estimates only.

Figure 9 shows an interesting trend in the data where, contrary to expectations, the DQE(0) for this detector is not constant but was found to vary with the detector signal. The trend persists when varying the detector signal by changing the photon flux (i.e. increasing the mA on the tube), as well as by increasing the integration time. We believe that this behavior may be related to the change in the detector gain, which increases slightly over the first 20% of the dynamic range.

An alternative method for estimating DQE(0) is given by Nishikawa et al.[4] Assuming that the detector does not add any significant amount of noise (i.e. the system is photon-noise limited), the DQE(0) is given by the product of A_Q, the quantum efficiency of the detector system, and A_S, the Swank factor[26] of the phosphor screen. A_Q, taking into account the thickness of the active layer in the Min-R Medium screen as well as absorption in the plastic backing and the protective graphite cover, is about 65% at 30 kVp for the RadEye1 system. A reasonable estimate for the Swank factor for Min-R Medium is 0.8.[27] This gives a theoretical DQE(0) of 52%, which is quite close to the measured values.

The noise power spectra shown in Figure 10 evidently scale well with the incident exposure, but don't fall off with frequency as quickly as one would expect from the MTF plots. As a result, the corresponding DQE curves in Figure 11 fall off to only 2% at the detector cutoff frequency. We believe that this behavior is caused by direct absorption of x-rays in the detector substrate. A small fraction of the incident photons are transmitted past the phosphor layer and subsequently absorbed in the

silicon substrate of the detector. Although these photons add to the total signal, they have an adverse effect on the signal-to-noise ratio since one of these photons will generate many more electrons than one absorbed in the scintillator. This results in an increase in the high-frequency noise power, since the MTF for the directly absorbed photons is that of the bare detector, which is more than three times the Min-R Medium MTF at 10 lp/mm. Another possible source of error is that the NPS curves have not been corrected for image non-uniformity from gain variations or changes in the x-ray intensity over the measured ROI. These are usually slow fluctuations that tend to decrease the DQE at low spatial frequencies.

5. APPLICATIONS

Typical applications for the RadEye1 detector include interventional mammography (needle biopsy), micro-angiography, bone densitometry and dental imaging. Although the current detector area is not yet large enough for full-field applications, it is quite sufficient for high-resolution region-of-interest imaging. In most of these applications a 5 cm by 5 cm tiled detector consisting of two RadEye1 imagers is used.

Figure 12 shows a resolution pattern made of 30 µm thick lead foil (Nuclear Associates P/N 07-539). This image was taken at 50 kVp using a Min-R Medium screen. The insert in the image shows that good contrast between the lead bars is maintained all the way up to 10 lp/mm. A slight discontinuity between the lead bars can be seen at the center of the image. This is where the gap between the two RadEye1 sensors is located. A larger gap (~200 µm) on this device causes a small shift in any linear features crossing it, because the gap-correction algorithm in the imaging software is calibrated to expect a two-pixel gap. A reduction in the gap size to 100 µm in the next generation of sensors is expected to eliminate this problem.

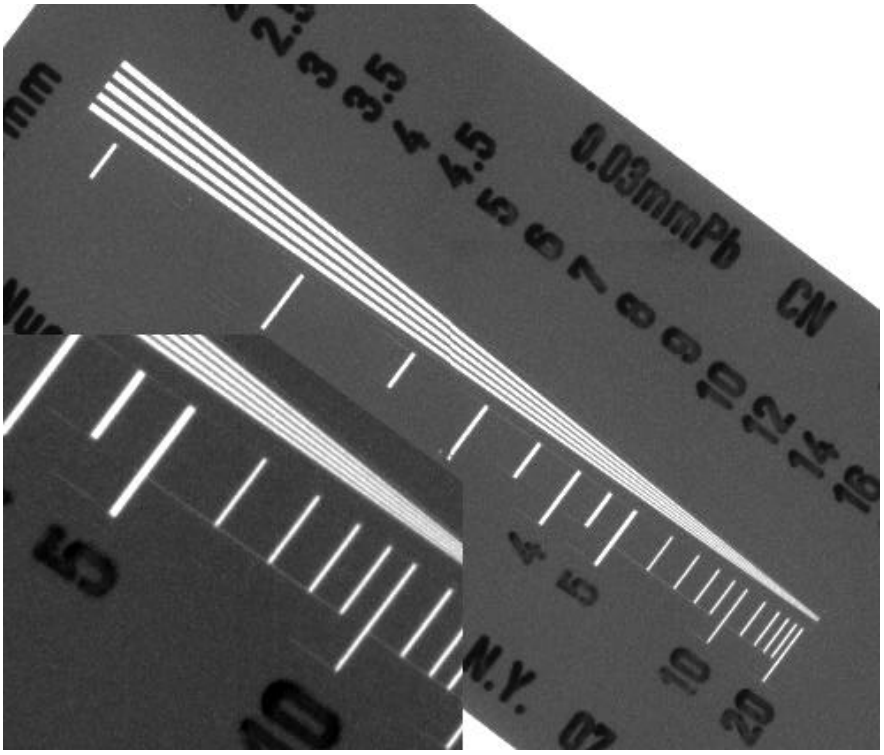

Figure 12 – Resolution pattern (50 kVp, Min-R Medium).

Figure 13 shows an example of a biological specimen imaged at 30 kVp with a Min-R Medium screen (50 mR exposure). Both the fine skeletal details and some of the soft tissue features can be discerned in the image.

Figure 13 – Biological specimen (30 kVp, Min-R Medium).

Finally, Figure 14 shows an image of an ACR accreditation phantom for stereotactic breast biopsy (Nuclear Associates P/N 18-250). This image was taken using a Tungsten target source at 25 kVp, 10 mAs, and without

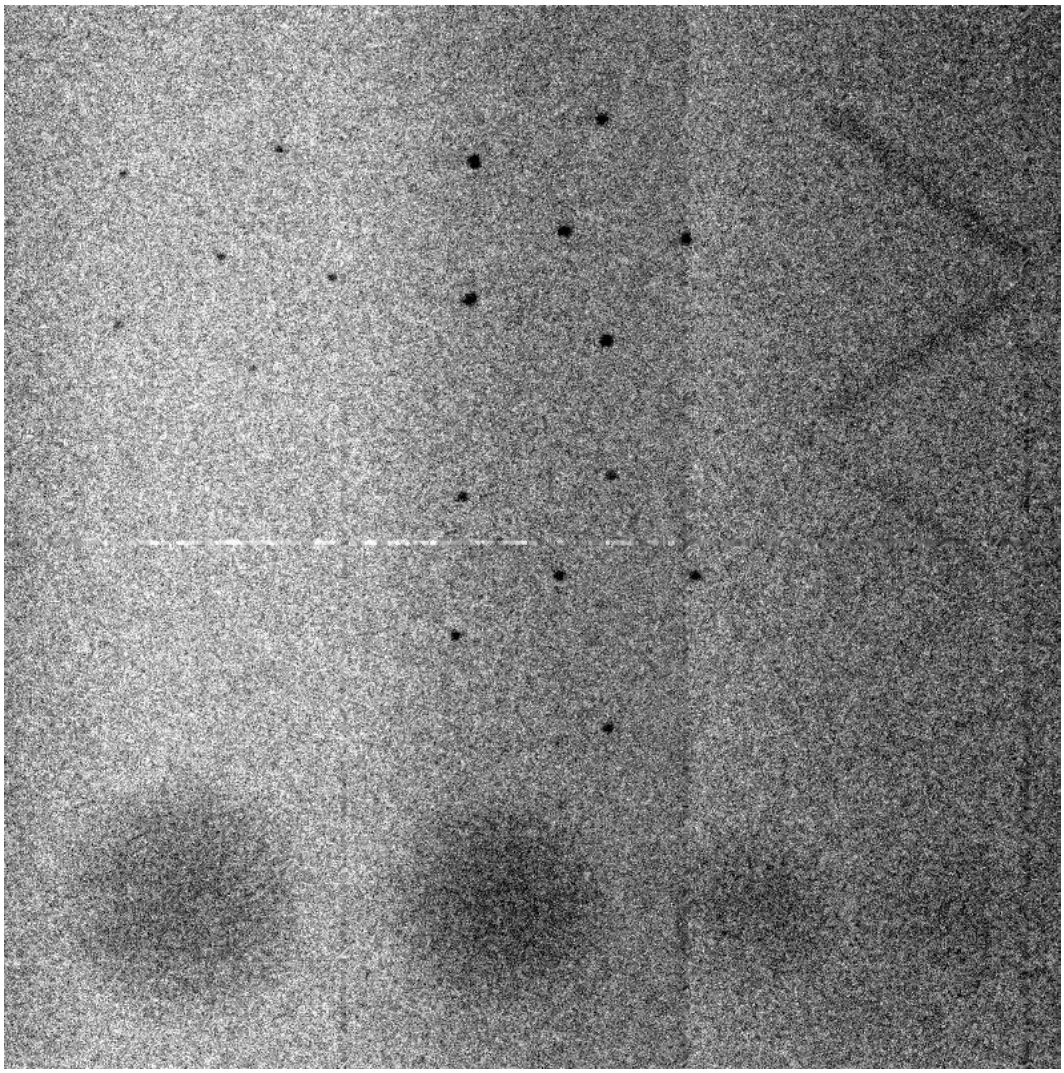

Figure 14 – ACR accreditation phantom for stereotactic breast biopsy.

any filtration other than a 125 μm Be window and the 35 cm air path. This spectrum is more energetic than a typical mammographic x-ray spectrum and is not quite optimized for this phantom. Nevertheless, it is possible to discern all of the relevant features in the image. The three visible speck groups range from 0.24 mm to 0.54 mm. A fourth 0.20 mm speck group is lost in the noise floor. Similarly, the three largest fibers of 0.54, 0.74 and 0.93 mm diameter can be seen in the right portion of the image, but there is not enough contrast to make out the fourth 0.32 mm diameter fiber. All four masses in the phantom, ranging from 0.25 mm to 1 mm thickness, can be observed along the bottom of the image. The slight left-to-right shading in the image is due to non-linearity in the gain correction for the imager.

6. CONCLUSION

There have been many studies describing the difficulties that confront the CMOS designer when shrinking the pixel size and hence the imager size to ever smaller dimensions. There exists a different, but equivalent set of somewhat obscure problems which must be addressed when increasing the imager size, as in the case of the RadEye1 imager. As is evident from the performance that is reported in this paper, Rad-icon has successfully disposed of these problems. The performance data presented in this report are comparable, if not better than those reported for many of the competing technologies.[17] Yet the higher integration, lower production cost, and simpler packaging requirements of the CMOS image sensor enable the development of low-cost, light-weight imaging solutions for the same applications.

It is also possible to extend the RadEye concept to even larger CMOS imagers in the future. CMOS technology is continuously expanding to larger wafer sizes. Six inch wafers allow the design of image sensors up to 100 mm long, which can be tiled to form up to 20 cm wide image planes. Eight inch wafers, which are becoming more widely available, and twelve inch wafers, which are starting to be introduced, would allow for even larger devices and image planes up to 30-40 cm. This technology development continues to be funded by the IC industry. As these trends continue to progress, CMOS technology will have a future in digital radiography.

REFERENCES

1. J.H. Siewerdsen, L.E. Antonuk and J. Yorkston, "Theoretical performance of amorphous silicon imagers in diagnostic radiology," *Proc. SPIE* **2708**, pp. 484-493, 1996.
2. R. Fahrig, J.A. Rowlands and M.J. Yaffe, "X-ray imaging using amorphous selenium: Detective quantum efficiency of photoconductive image receptors for digital mammography," *Med. Phys.* **22**, 153-160, 1995.
3. M.P. Andre, B. Spivey, P. Martin, L. Morsell, E. Atlas and T. Pellegrino, "An integrated CMOS-Selenium x-ray detector for digital mammography," *Proc. SPIE* **3336**, pp. 204-209, 1998.
4. R.M. Nishikawa, G.E. Mawdsley, A. Fenster and M.J. Yaffe, "Scanned projection digital mammography," *Med. Phys.* **14**, pp. 717-727, 1987.
5. G.S. Shaber, C. Lockard and J.M. Boone, "High resolution digital radiography utilizing CCD planar array," *Proc. SPIE* **914**, pp. 262-269, 1988.
6. A. Karellas, H. Liu, L.J. Harris and C.J. D'Orsi, "Operational characteristics and potential of scientific-grade charge-coupled devices in x-ray imaging applications," *Proc. SPIE* **1655**, pp. 85-91, 1992.
7. A.D.A. Maidment and M.J. Yaffe, "Analysis of the spatial-frequency-dependent DQE of optically coupled digital mammography detectors," *Med. Phys.* **21**, pp. 721-729, 1994.
8. S.T. Smith, D.R. Bednarek, D.C. Wobschall, M. Jeong, H. Kim and S. Rudin, "Evaluation of a CMOS image detector for low cost and power medical x-ray imaging applications," *Proc. SPIE* **3659**, pp. 952-961, 1999.
9. J.M. Herron, W.H. Kennedy, D. Gur, S.L. Miller, W.F. Good, B.C. Good, R.E. Latchaw and H. Yonas, "X-ray imaging with two-dimensional charge-coupled device (CCD) arrays," *Proc. SPIE* **486**, pp. 141-145, 1984.
10. J.M. Herron, E.G. Daxon, D. Gur, W.F. Good, G.S. Maitz and S.L. Miller, "X-ray imaging with 2048 x 2048 CCD array," *Proc. SPIE* **1231**, pp. 374-380, 1990.
11. A.D.A. Maidment, M.J. Yaffe, D.B. Plewes, G.E. Mawdsley, I.C. Soutar and B.G. Starkoski, "Imaging performance of a prototype scanned-slot digital mammography system," *Proc. SPIE* **1896**, pp. 93-103, 1993.
12. D. Rosen, W. Phillips, M. Stanton, J. Xie, D. O'Mara and A. Stewart, "A prototype CCD-based detector for whole breast digital mammography," *Proc. SPIE* **3032**, pp. 52-58, 1997.
13. S. Thunberg, H. Sklebitz, B. Ekdahl, L. Baetz, A. Lundin, H. Moeller, F. Fleischmann, G. Kreider and T. Weidner, "OPDIMA: Large-area CCD-based X-ray image sensor for spot imaging and biopsy control in mammography," *Proc. SPIE* **3659**, pp. 150-158, 1999.
14. S. Rudin, D.R. Bednarek, A.K. Wakhloo, B.B. Lieber, C.J. Yang and D. Nazareth, "Region of interest micro-angiography: radiographic imaging optimized for vascular interventions," *Proc. SPIE* **3659**, pp. 708-717, 1999.
15. A. Karellas, L.J. Harris, H. Liu, M.A. Davis and C.J. D'Orsi, "Charge-coupled device detector: Performance considerations and potential for small-field mammographic imaging applications," *Med. Phys.* **19**, pp. 1015-1023, 1992.
16. H. Roehrig, L. Fajardo and T. Yu, "Digital X-ray cameras for real-time stereotactic breast needle biopsy," *Proc. SPIE* **1896**, pp. 213-224, 1993.
17. H. Roehrig, L.L. Fajardo, T. Yu and W.S. Schempp, "Signal, noise and detective quantum efficiency in CCD based x-ray imaging systems for use in mammography," *Proc. SPIE* **2163**, pp. 320-332, 1994.
18. L. Mortara and A. Fowler, "Evaluations of charge-coupled device (CCD) performance for astronomical use," *Proc. SPIE* **290**, pp. 28-33, 1981.
19. P.F. Judy, "The line spread function and modulation transfer function of a computed tomographic scanner," *Med. Phys.* **3**, pp. 233-236, 1976.
20. S.E. Reichenbach, S.K. Park and R. Narayanswamy, "Characterizing digital image acquisition devices," *Opt. Eng.* **30**, pp. 170-177, 1991.
21. H. Fujita, D. Tsai, T. Itoh, K. Doi, J. Morishita, K. Ueda and A. Ohtsuka, "A simple method for determining the modulation transfer function in digital radiography," *IEEE Trans. Med. Imaging* **11**, pp. 34-39, 1992.
22. J.M. Boone, "Spectral modeling and compilation of quantum fluence in radiography and mammography," *Proc. SPIE* **3336**, pp. 592-601, 1998.
23. R. Birch, M. Marshall and G.M. Ardran, *Catalogue of spectral data for diagnostic x-rays*, Hospital Physicists' Association, London, 1979.
24. J.C. Dainty and R. Shaw, *Image science: principles, analysis and evaluation of photographic-type imaging processes*, Chapter 6, Academic Press, New York, 1974.
25. J.T. Dobbins, D.L. Ergun, L. Rutz, D.A. Hinshaw, H. Blume and D.C. Clark, "DQE(f) of four generations of computed radiography acquisition devices," *Med. Phys.* **22**, pp. 1581-1543, 1995.
26. R.K. Swank, "Absorption and noise in x-ray phosphors," *J. Appl. Physics* **44**, pp. 4199-4203, 1973.
27. D.P. Trauernicht and R. Van Metter, "The measurement of conversion noise in x-ray intensifying screens," *Proc. SPIE* **914**, pp. 100-116, 1988.